Article

Not peer-reviewed version

High Energy Pulsed Laser Beam to Produce a Thin Layer of Crystalline Silver without Heating the Deposition Substrate and Its Catalytic Effects

Alexandru Cocean , Georgiana Cocean , Cristina Postolachi , Silvia Garofalide , Daniela Angelica Pricop , Bogdanel Silvestru Munteanu , Georgiana Bulai , Nicanor Cimpoesu , Iuliana Motrescu , Vasile Pelin , Razvan Vasile Ababei , Dan-Gheorghe Dimitriu * , Iuliana Cocean , Silviu Gurlui *

Posted Date: 28 March 2024

doi: 10.20944/preprints202403.1717.v1

Keywords: catalysis; ablation plasma diagnosis; borax treatment

 doi:10.20944/preprints202403.1717.v1

Article

High Energy Pulsed Laser Beam to Produce a Thin Layer of Crystalline Silver without Heating the Deposition Substrate and Its Catalytic Effects

Alexandru Cocean [1,2], Georgiana Cocean [1,3], Cristina Postolachi [1], Silvia Garofalide [1,2], Daniela Angelica Pricop [1,4], Bogdanel Silvestru Munteanu [1], Georgiana Bulai [5], Nicanor Cimpoesu [1,6], Iuliana Motrescu [7], Vasile Pelin [1,2], Razvan Vasile Ababei [1,4], Dan-Gheorghe Dimitriu [1,*], Iuliana Cocean [1] and Silviu Gurlui [1,*]

[1] Atmosphere Optics, Spectroscopy and Laser Laboratory (LOASL), Faculty of Physics, Alexandru Ioan Cuza University of Iasi, 11 Carol I Blvd., 700506 Iasi, Romania; alexcocean@yahoo.com (A.C.), cocean.georgiana@yahoo.com (G.C.), tina.postolaki@gmail.com (C.P.), silvia.garofalide90@gmail.com (S.G.), daniela.a.pricop@gmail.com (D.A.P.), muntb@uaic.ro (B.S.M.), nicanor.cimpoesu@tuiasi.ro (N.C.), vasile.pelin@uaic.ro (V.P.), razvan.ababei@uaic.ro (R.V.A.), dimitriu@uaic.ro (D.G.D.), iuliacocean@gmail.com (I.C.), sgurlui@uaic.ro (S.G.)

[2] Laboratory of Applied Meteorology and Climatology, Research Center with Integrated Techniques for Atmospheric Aerosol Investigation in Romania, RECENT AIR, Alexandru Ioan Cuza University of Iasi, 11 Carol I Blvd., 700506 Iasi, Romania;

[3] Rehabilitation Hospital Borsa, 1 Floare de Colt Str., 435200 Borsa, Romania;

[4] Laboratory of Astronomy and Astrophysics, Astronomical Observatory, Research Center with Integrated Techniques for Atmospheric Aerosol Investigation in Romania, RECENT AIR, Alexandru Ioan Cuza University of Iasi, 11 Carol I Blvd., 700506 Iasi, Romania;

[5] Integrated Centre of Environmental Science Studies in the North Eastern Region (CERNESIM), Department of Exact and Natural Sciences, Institute of Interdisciplinary Research, Alexandru Ioan Cuza University of Iasi, 11 Carol I Blvd., 700506 Iasi, Romania; georgiana.bulai@uaic.ro

[6] Faculty of Material Science and Engineering, Gheorghe Asachi Technical University of Iasi, 59A Mangeron Blvd., 700050 Iasi, Romania;

[7] Sciences Department & Research Institute for Agriculture and Environment, Iasi University of Life Sciences, 3 Sadoveanu Alley, 700490 Iasi, Romania; imotrescu@uaiasi.ro

* Correspondence: dimitriu@uaic.ro (D.G.D.) and sgurlui@uaic.ro (S.G.)

Abstract: Crystalline silver thin layers were obtained by high-energy pulsed laser ablation without heating of the deposition substrate. The fluid Plateau-Rayleigh (PRI), Rayleigh – Taylor (RTI) and Richtmyer – Meshkov (RMI) instabilities, as well as crown splash induced during pulsed laser deposition (PLD) in high energy regime, resulting in ring and pearl shaped structures, offer the benefit of increased sorption surface. These morphological structures obtained for the silver thin layers make them of interest for catalytic applications. The study presented with this work addresses both the fundamental and applied issues on the morphological structures obtained for the silver thin layer and their catalytic function in organic processes. In this sense, the catalytic action of the thin silver layer was highlighted by modifications of the Reactive Blue 21 dye (C.I.) in aqueous solution with sodium bicarbonate. Specific investigations and analyzes were carried out by electron microscopy and elemental analysis (SEM-EDX), atomic force microscopy (AFM) and profilometry, mass spectrometry, ablation plasma diagnosis, diffractograms (XRD), as well as IR spectroscopy (FTIR). In addition to the experimental investigation and analyzes, simulation of the ionization energy threshold was conducted in COMSOL for complementary evaluation on the involved processes and phenomena.

Keywords: catalysis; ablation plasma diagnosis; borax treatment

 doi:10.20944/preprints202403.1717.v1

1. Introduction

Laser ablation has been intensively studied since the 60s, with the beginnings of the development of laser techniques and its application in LIBS and LIF spectroscopy [1,2]. The investigation of the physico-chemical phenomena developed both at the level of the target in the interaction with the laser beam and of the ablation plume was carried out by developing techniques to analyze the composition of the target and capture the dynamics of the plume by using ICCD camera, Langmuir probe, LIBS spectroscopy (Laser Induced Breakdown Spectroscopy), LIF (Laser Induced Fluorescence) etc. [1–10]. Due to the very short laser pulse width (nanoseconds, femtoseconds), some parameters could not be measured, such as the temperature reached when the laser radiation interacts with the target. The development of numerical models and numerical simulation have replaced this technical impediment [11–13]. While for pure metal targets the analysis of plasma components is reduced to the nature of charged, neutral or aggregated species in the form of so-called clusters, for targets made of metals with impurities, alloys or chemicals of greater complexity, the chemical analysis of the ablation plume is harder to achieve. In the analysis using laser ablation, the Laser Ablation Inductively Coupled Plasma Mass Spectrometry technique has been developed and used so far [14–18]. This technique only addresses the analysis of the target material. However, mass spectroscopy has not yet been used directly for ablation plume analysis because laser ablation is not sufficient to reach the ionization energy. As shown in previous studies, laser ablation produces liquid and gas phases, as well as a smaller amount of the ionized phase (plasma) [9–12]. The current study aims to increase the ionization rate in laser ablation using previous chemical treatments of the target.

Plasma of ablation has been previously investigated using optical imaging techniques [8,19,20]. Silver thin films obtained by PLD technique have been described as the result of nanoparticles deposition [9,11,12]. Pulsed Laser Deposition (PLD) using silver target has been treated from the perspective of fluid model of ablation plasma. Plateau-Rayleigh (PRI), Rayleigh – Taylor (RTI) and Richtmyer – Meshkov (RMI) instabilities, as well as crown splash have been reported [12]. Therefore, thin metallic films roughness obtained due to the fluid instabilities can be interpreted as the result of the last micro and nanoparticles deposited during PLD process and which are not in a sufficient number/quantity to form a compact continuous layer [12]. Therefore, thin films with high roughness are potential materials to be used in sorption processes and catalytic processes.

The novelty of the study presented with this work consists in a complex analysis of the phenomena and physico-chemical processes that take place during the pulsed laser deposition of a thin layer of silver with impurities, as well as of those arising from the interaction of the thin layer with complex organic molecules in the sense of the catalytic effect. In the analysis of the ablation plasma plume, the novelty consists in obtaining information on the developed chemical species using mass spectroscopy and the pulsed laser as source of ionization energy of the chemical species.

2. Materials and Methods

2.1. Materials

The silver thin film (Ag-thin film) was obtained from the target of silver containing iron and nickel impurities of jewelry provenience. The target was produced using thermal and chemical procedures as described in our previous papers [12,13]. Sodium tetraborate ($Na_2B_4O_7 \cdot 10H_2O$) and sodium borohydride ($NaBH_4$) were used to convert metals cations from oxides and hydroxides into their atomic state [21,22], while the sulfur from silver sulfide (Ag_2S) was removed with sodium bicarbonate and aluminum foil. Specifications for the component elements of the target are shown in Table 1.

 doi:10.20944/preprints202403.1717.v1

Table 1. Characteristics of the target component elements [23–27].

Element	Melting point (K)	Boiling point (K)	Atomic mass (a.m.u.)	Atomic number	Heat of vaporization (kJ/mol)	Ionization energy (eV)
Ag	1234	2435	107.8682	47	254	7.5762
Fe	1811	3134	55.845	26	340	7.9024
Ni	1728	2002	58.6934	28	379	7.6398
B	2349	4200	10.811	5	508	8.29803

The aqueous solution of C.I. Reactive Blue 21 (10 g/L) and $NaHCO_3$ (10 g/L) (RB21) was prepared and used to test the Ag thin film catalytic properties in decomposition of the residual textile dyestuff from industrial wastewaters.

2.2. Method of Work

The target was used in the Pulsed Laser Deposition (PLD) process for producing thin films and for plasma dynamics and composition investigation, using YG 981E/IR-10 laser system, Q-switched Nd:YAG laser, laser beam wavelengths (λ) domains: visible at 532 nm (Vis); ultraviolet at 355 nm and 266 nm (UV) and 1064 nm infrared (IF), in pulses of 9 - 10 ns with a repetition frequency of 10 Hz and with energies of 1–150 mJ/pulse, producer Quantel, Les Ulis, France. The silver target was ablated using this system at the following parameters and conditions: τ = 10 ns pulse width, λ = 532 nm wavelength, α = 45° incident angle and ν = 10 Hz pulse repetition time. The pressure in the deposition chamber was $3 \cdot 10^{-2}$ Torr and the deposition support was placed at 2 cm distance from the target. Laser fluency of F = 50 mJ/cm^2 (E = 180 mJ; r = 336 μm). The setup is schematically represented in Figure 1 and it includes the ICCD camera and the mass spectrometer.

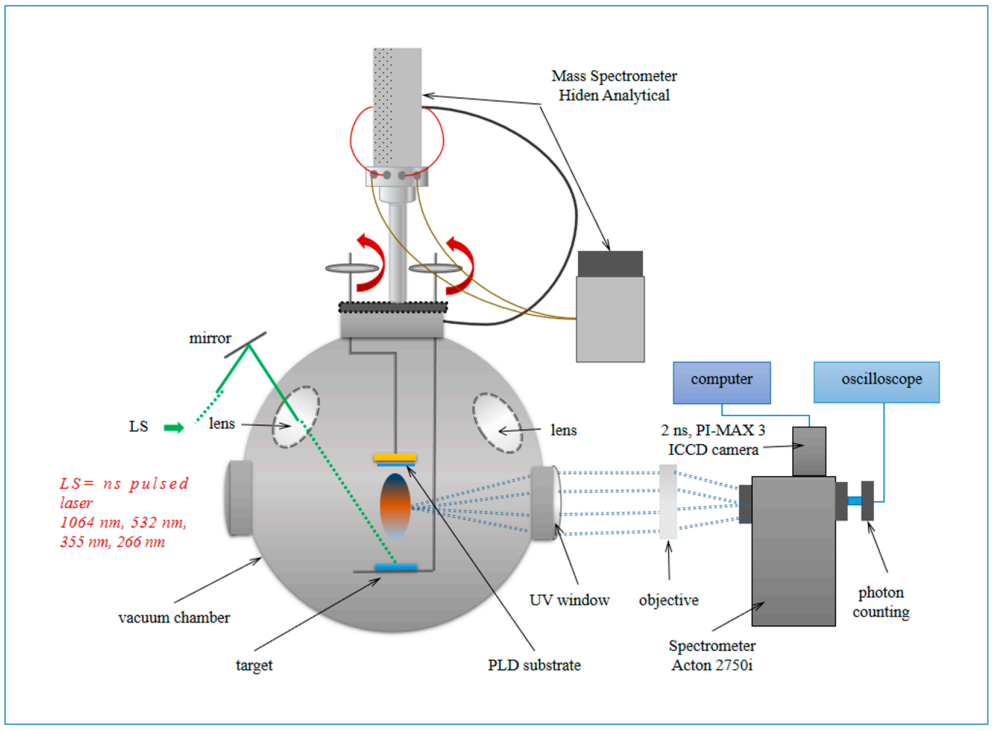

Figure 1. Experimental set-up of PLD installation with YG 981E/IR-10 laser system (LS), vacuum chamber, PI-MAX 3 ICCD camera and Mass Spectrometer for monitoring plasma of ablation (Atmosphere Optics, Spectroscopy and Lasers Laboratory).

 doi:10.20944/preprints202403.1717.v1

The catalytic test was performed as follows: 0.5 ml of RB21 solution was poured on the silver thin film deposited on a glass slab. The same quantity of RB21 solution was poured on a glass slab as control test. The dry resulting materials on the Ag-thin films are denoted as R-Ag, while the resulting materials from solution leakage after interaction with the thin film and after drying are denoted as Q-Ag. The control test consisting in dried RB21 solution deposited on the glass slab is denoted as RB21-$NaHCO_3$.

2.3. Methods of Analysis

The morphology of the thin film surface was analyzed by scanning electron microscopy coupled with energy dispersive X-Ray spectroscopy using the SEM-EDX Vega Tescan LMH II, Brno, Czech Republic. For electron spectroscopy, an SE detector was used at 30 kV filament supply and a working distance of 15.5 mm. Bruker detector X-Flash 6/30 with Automatic mode detection, precise experiment was used on EDX analysis.

The topography was studied by Atomic Force Microscopy (AFM), Nanosurf Easy Scan 2, Liestal, Switzerland, AFM contact mode, cantilever n+ - silicon with resistivity 0.01-0.02 Ωcm, thickness 2±1 μm and force constant 0.02-0.77 N/m.

The recorded images were resolved in space and time using a sequential imaging technique with exposure time (integration) and delays varied in the nanosecond range. The camera with CCD intensification (Roper Scientific ICCD 2ns Pi-Max 3 – 1024i camera) has an integration time of 2 ns and a resolution of 1024×1024 pixels. In the experiment, an integration time of 3 ns was chosen, while the images were recorded after the laser pulse, from 100 ns to 1200 ns, for each image 10 acquisitions being made.

The elemental composition of the ablation plasma was studied with Mass Spectrometer HAL RC9 (2U), Hiden Analytical Ltd., UK.

Fourier Transform Infrared spectroscopy analysis was performed with FT-IR Spectrometer Bomem MB154S at an instrumental resolution of 4 cm^{-1} (Bomem, ABB group, Canada) on the samples of RB21 dried material collected from the surface of the thin film and of the solution that leaked from the thin film, as well as from the control test.

Profilometry was performed with DektakXT stylus profilometer (Bruker, Bruker Nano Surfaces Division, 3400 East Britannia Drive, Suite 150, Tucson, AZ 85706), with a repeatability of 4 Å, on the Ag thin film after washing the dried material resulted after treating the thin films with the RB21 solution, and the thinness and roughness of the thin films after treatment was compared with the thinness before treatment.

The crystalline structure of the Ag-thin film was analyzed by X-ray diffraction using a Shimadzu LabX XRD-6000 Diffractometer with a Cu Kα radiation (λ = 1.54 Å). The diffraction patterns were recorded in the 10° – 80° 2θ range with a 2 deg/min scanning speed.

Numerical simulation was conducted in COMSOL 5.6 - 01 software version (COMSOL AB, Stockholm, Sweden).

3. Results and Discussion

Monitoring with the ICCD 2 ns Pi-Max 3 camera during pulsed laser deposition (Figure 2) allowed the calculation of the speed of the ablation plume as being of 6.5 x 10^3 m/s. Based on the same measurements, a periodical plasma layered structure was highlighted at about 1 mm from target, 447 ns delay, with the distance between two layers of particles approximately the same, of 0.06 mm. This phenomenon could be assigned to a perturbation materialized in the electric field of diffusion of the diffusion current generated by the charged carriers in the plasma plume in motion and in the shock wave developed under the very high velocity plasma plume.

 doi:10.20944/preprints202403.1717.v1

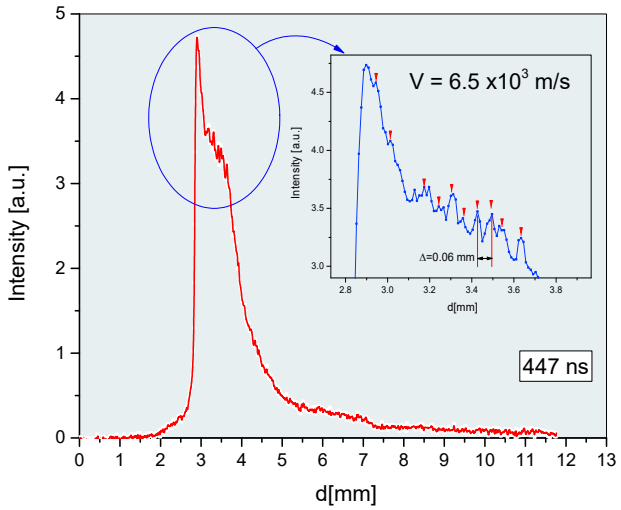

Figure 2. Distribution of global intensity of laser ablation plasma.

The number of species (atoms, ions, crystalline structures, etc.) developed in the ablation plasma during its movement and the phenomena of recombination, crystal growth and cooling were also considered. In this sense, analyzes were carried out with the mass spectrometer connected to the deposition installation. For the analysis of the ablation plume's composition, an energy of 30 mJ of 532 nm laser beam was used in a pulsed regime of 10 ns and 100 Hz repetition frequency, this being at the same time the source of ionization of the component chemical species. The elements silver, iron, nickel and boron were identified as results according to the spectral lines in the spectra presented in Figure 3.

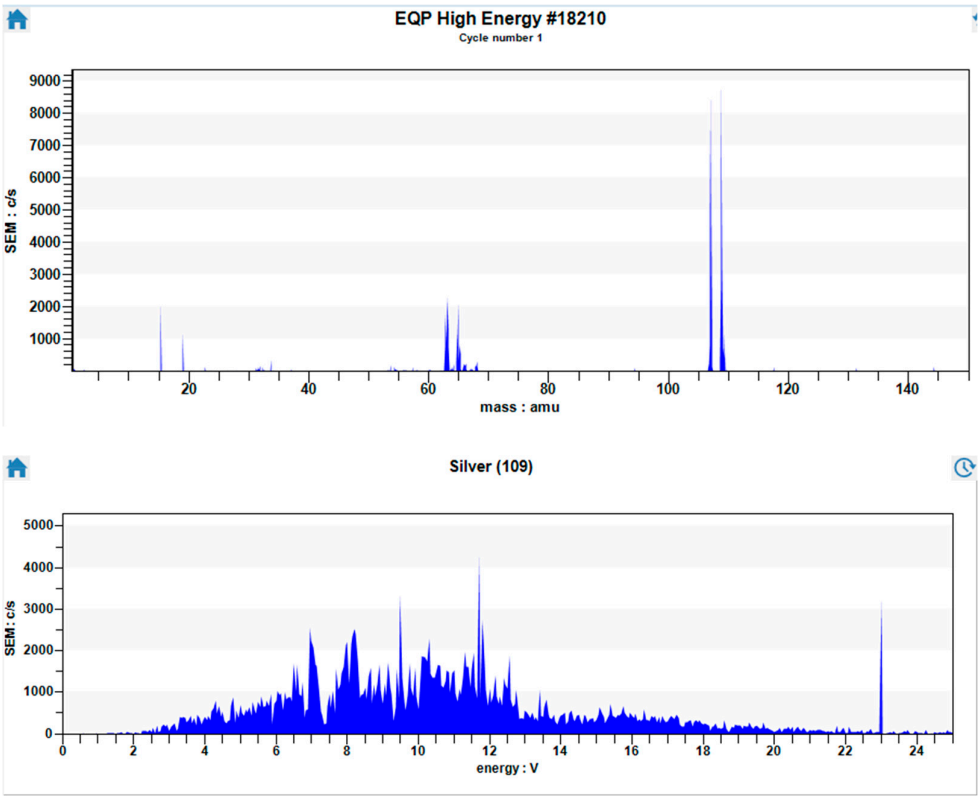

 doi:10.20944/preprints202403.1717.v1

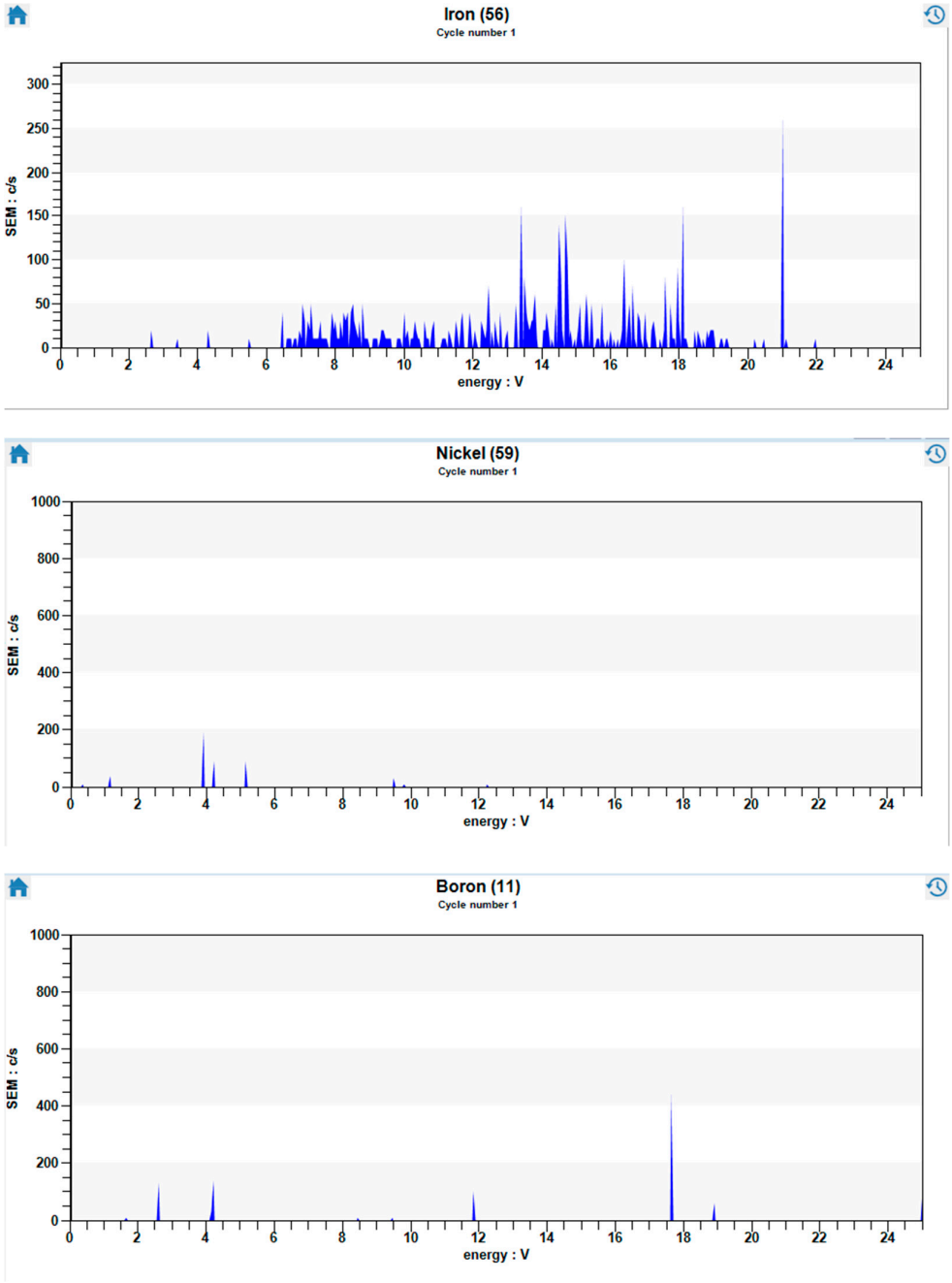

Figure 3. Mass Spectrometry determination of the elemental composition of the ablation plasma.

Reaching an ionization level of silver atoms is located after a significant time interval, namely 100 μs, as it results from the 3D diagram obtained during the analysis with the mass spectrometer (Figure 4).

 doi:10.20944/preprints202403.1717.v1

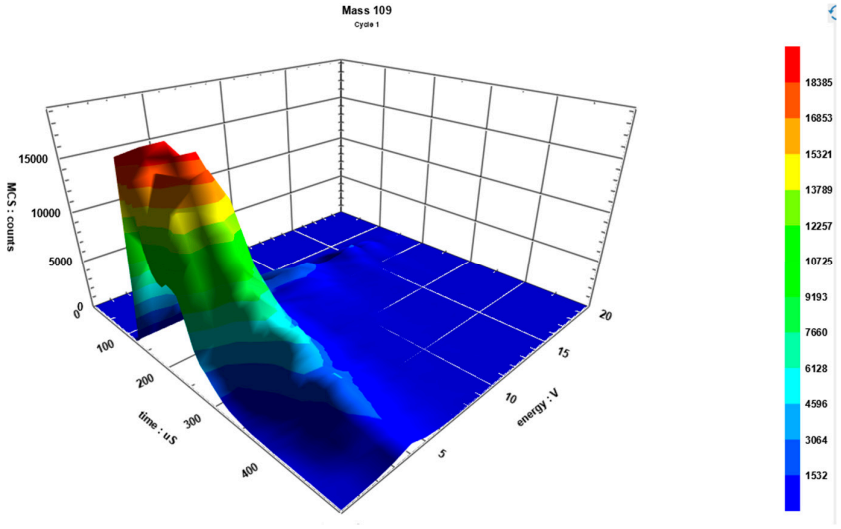

Figure 4. 3D Silver ions developed in time at different values of the energy.

The composition of the ablation plume corresponds to the results of the analysis of Ag target with Fe and Ni impurities, which was treated with boron-based compounds. The EDX analysis of the target was presented in our previous works as being on two analyzed areas of 64.56% Silver, 27.01% Nickel, 8.43% Iron and of 77.20% Silver, 17.56% Nickel, 5.20% Iron, respectively. In addition, the mass spectrometry also highlighted the presence of boron which was expected according to the treatments during the fabrication of the target.

In order to understand the phenomena that contributed to the ionization of the chemical species in the silver target with impurities, used in the laser ablation process, a simulation was conducted in COMSOL 5.6. The mathematical model and its implementation in the Heat Transfer module were made according to [11,12,28], and the parameters in the simulation were the same as the laser parameters used during the analysis with the mass spectrometer. The results obtained by simulation are presented in the form of ionization energy threshold (IET) diagrams in Figure 5. According to Table 1 and plots of Figure 5e,f, the threshold of ionization energies is reached and exceeded even after a single laser pulse for the elements iron (maximum achieved of 77.9 eV compared to IET of 7.9024 eV), nickel (maximum achieved of 48.5 eV compared to IET of 7.98 eV), boron (maximum achieved of 270 eV compared to IET of 8.298 eV). In the case of silver, the simulation indicates thermal energies of 0.62 eV (Figure 5d) developed under the action of one laser pulse, which is below the ionization energy threshold level of 7.5762 eV. Furthermore, the analysis of the simulation results was performed for a time of 2 μs from the ignition of the laser pulse, as much as the processing memory of the computer allowed in the context where the data acquisition is very large, i.e., a large number of reading nodes given by extra fine mesh required. From the extended diagrams for the duration of 2 μs from the ignition of the laser pulse, it appears that, in the presence of boron, each of the elements silver, iron and nickel, respectively, changes its thermal behavior in the sense of extending the heating effect of the ablation plasma. In this sense, although the thermal energy decreases during the laser pulse, the residual thermal energy will improve the thermal effect of the next laser pulse. This phenomenon leads to the idea that the generation of silver ions under low pulsed laser energy is influenced by the presence of boron or boron compounds present in residual form after introduced during the processing of the target.

 doi:10.20944/preprints202403.1717.v1

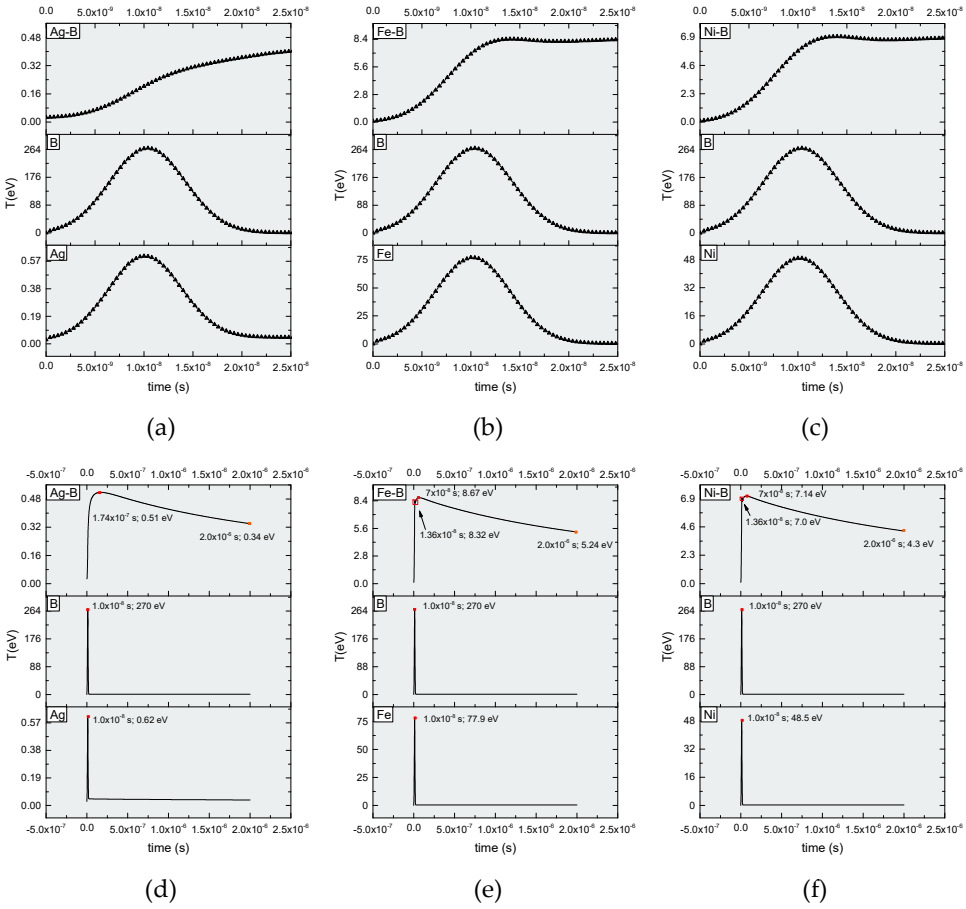

Figure 5. COMSOL simulation of the thermal energy developed during ablation after one laser pulse evaluated during 20 ns (a, b, c) and during 2000 ns (d, e, f).

Returning to the optical images of layered structures obtained with the ICCD camera, that could be in connection with the analysis of the ablation plume with mass spectrometry, which indicates a large number of neutral and charged chemical species (atoms and ions of silver, iron, nickel, boron, as well as different combinations of Ag-B, Fe-B, Ni-B etc.).

The diffractogram obtained from the XRD analysis of the thin film deposited from the Ag target (Ag-thin film) shows its polycrystalline structure (Figure 6). The X-Ray diffraction analysis on the Ag-thin film evidenced the crystalline specific sharp peaks and Miller indices as (111), (200), (220) and (311), as in literature [28–32]. Since the deposition was performed on a glass substrate at ambient temperature (without heating), it means that the crystalline structure was formed in the ablation plume, by crystal growth. Silver crystalline states in different crystal growth stages could also contribute to the optical images of the plume of ablation as layered structures of Figure 2.

 doi:10.20944/preprints202403.1717.v1

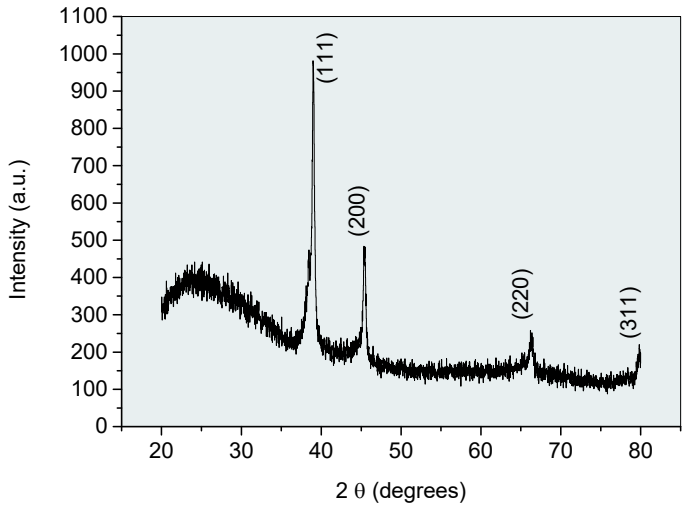

Figure 6. Silver layer XRD diffractogram.

In the images obtained by SEM and AFM analysis (Figure 7), a morphology consisting of rings and droplets as well as their aggregates is noticeable. Formations with sizes ranging from 2.9 μm to 0.801 μm and even smaller for rings were measured, and in the case of droplets the sizes vary from 2.403 μm to 0.133 μm and even smaller. These indicate the formation of nanoparticles, as well as micrometric structures, some resulting from the aggregation of smaller particles, while others as melt splashes.

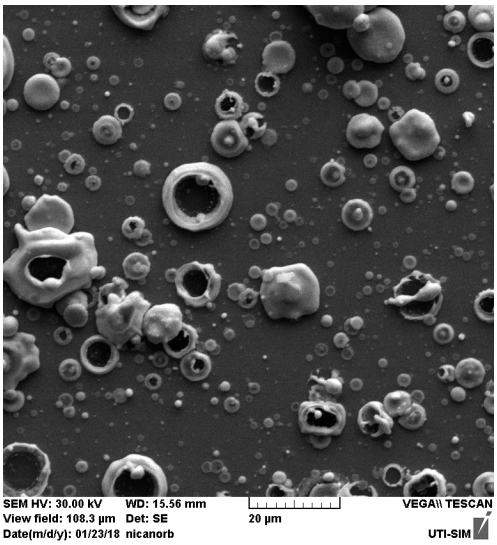

(a)

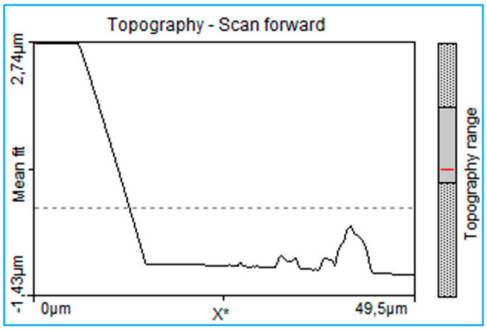

(b)

 doi:10.20944/preprints202403.1717.v1

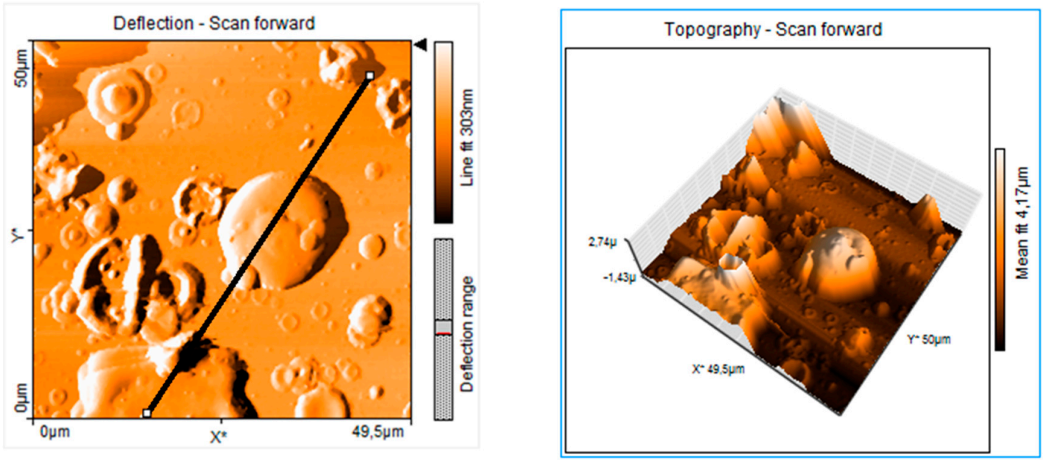

(c) (d)

Figure 7. Morphology and topography of the Ag-thin films: images with droplets and rings on the Ag-thin film surface by SEM (a) and AFM (b,c,d).

This morphology of the thin metallic films indicates, as previously mentioned [12], the instabilities in the fluid phases during ablation and plasma plume motion from target to support, which consist in the following phenomena and processes that are schematically represented in Figure 8.

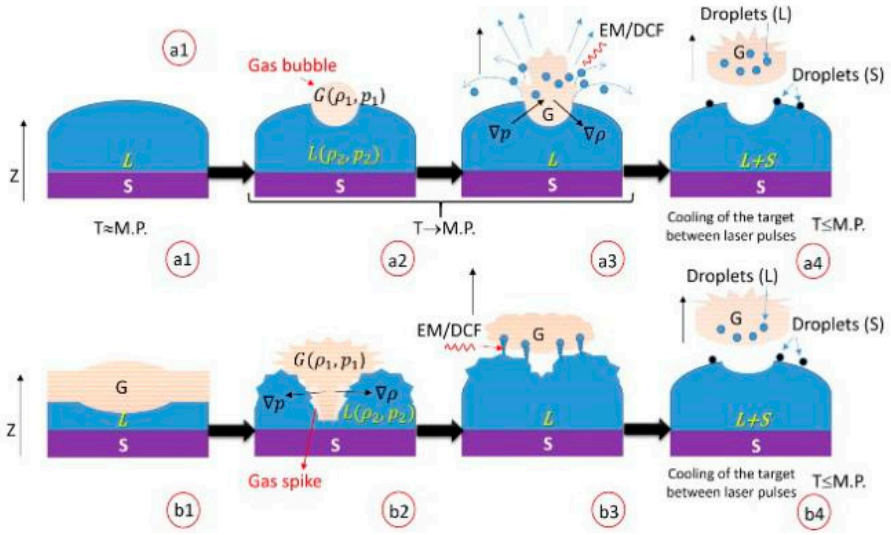

 doi:10.20944/preprints202403.1717.v1

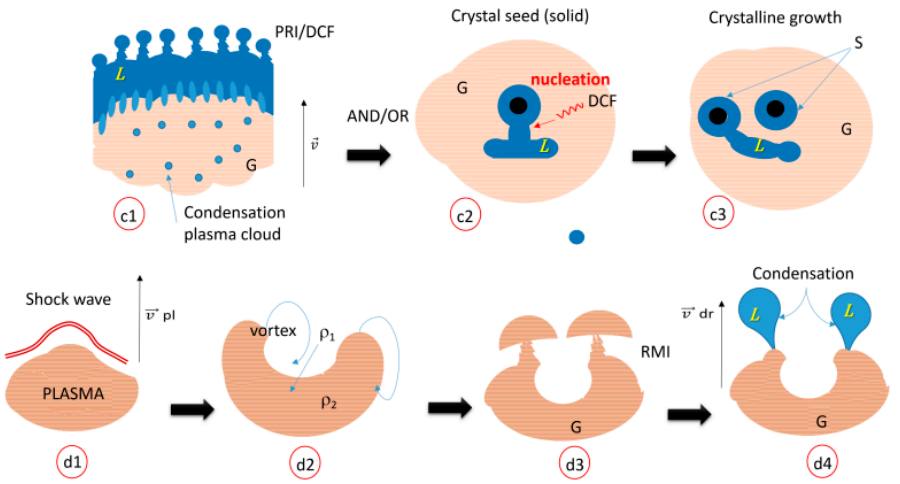

L = liquid state	**p = pressure**
G = gas/plasma state	**∇p = pressure gradient**
M.P. = melting point	**PRI = Plateau – Rayleigh instability**
B.P. = boiling point	**RTI = Rayleigh – Taylor instability**
EM = laser beam electromagnetic field	**RMI = Richtmyer – Meshkov instability**
DCF = electric field of diffusion current	**v_{dr} = droplet velocity**
ρ = density	**v_{pl} = plasma velocity**
$\nabla \rho$ = density gradient	**= perturbation sign**

Figure 8. Schematic representation of instabilities in the fluid phases during ablation and plasma plume motion from target to support: RTI on the target melted area where temperature is near boiling point (a); RTI at the interface between plasma/gas layer and the melted phase below it (b); PRI in the clouds of condensation formed during plasma plume motion from target to the support (c); RMI developed into the plasma plume under the shock wave developed during its motion with high speed (d).

a) One of the instabilities, a RTI type, occurs to liquid - gas interface in the areas on the target with temperatures near the boiling point (Figure 8 a1), when gas phase starts to develop into the liquid phase in a bubbling phenomenon. The bubbles of lower density than the melted phase will tend to develop in volume, being at the same time compressed by the liquid phase and a pressure gradient will be generated, where $p_{gas} > p_{liquid}$ while $\varrho_{gas} < \varrho_{liquid}$, fulfilling the condition (1): $\nabla\rho \cdot \nabla p < 0$ [26]. The pressure and density gradients will generate the perturbation responsible for the RTI and the gas bubbles will leave the liquid phase generating also a splash of liquid (Figure 8 a4). The liquid streams splashed under PRI will break-up into droplets for unstable modes (induced under the laser beam electromagnetic field and the electric field of diffusion current) when $k \cdot R_0 < 1$, where k is the wave number. The fastest growing modes occurs for $k \cdot R_0 = 0.697$, when the wavelength of the disturbance is $\lambda_{max} \cong 9.02 \cdot R_0$ [33,34].

b) The other situation were an instability of RTI kind is developed is on the areas of the target where on the irradiated surface the temperature highly exceeds the boiling point, so that a plasma/gas layer develops on a melted layer (Figure 8 b1). The plasma/gas will expend the volume in both directions, toward the support, but also toward the target, and, in the latter case, a deformation inside melted material will be induced, continuing to "dig" as a spike shape hole filled with gas (Figure 8 b2). The side melted material will be under a stress that will be released at the liquid-gas interface in the immediate vicinity, generating again (like situation "a") a splash of liquid (Figure 8 b3) that, crossing the plasma, will be under the perturbing effects of the electric field of the diffusion current induced by charged carriers, leading to the liquid streams break-up into droplets (Figure 8 b4), under the same conditions presented in paragraph (a).

 doi:10.20944/preprints202403.1717.v1

c) Figure 8c schematically represents the same type of RTI instability as in paragraph b) that occurs in target areas where temperature values are close to boiling points only at the boundary between the liquid phase and the plasma/gas phase developed on the irradiated surface of the target. The pressure in the plasma/gas phase is increased by the thermal effect and phase change, the plasma/gas phase tending to consume its volume and, with the pressure and density gradients under conditions from paragraph (a), will develop an inward peak. The melt will be directed towards the neighboring molten zone, generating on the one hand flows and droplets in the gas/plasma zone (Figure 8 c1) as a PRI-type instability, and, on the other hand, gas bubbles will form in the molten zone and they will continue to move into the liquid mass in the region of lowest pressure at the interface of the liquid phase with the ambient atmosphere, where in the meantime the ablation plasma "cloud" should have already expanded, lowering the pressure as well and providing the carriers charge to generate the diffusion electric field. The escape of the gas from the bubbles in the liquid mass will be accompanied by a kind of volcanic eruption, in a splash nozzle-less spray when the droplets are generated as PRI under the electric field of the diffusion current disturbance. A fraction of the droplets generated under the conditions described in paragraphs (a), (b) and (c) will be re-deposited, while another fraction will be entrained in a nozzle with less spray effect in the ablation plasma plume, contributing to the following phenomena and processes, including elastic collisions and return on the target or deposition on the walls of the vacuum chamber, but also moving with the plasma plume to the deposition support and becoming seeds for a new nucleation process in droplets in contact with the resulting liquid phase during plasma/gas condensation, before or in the support quarter. The complex phenomena of droplet generation in the PLD process continue with the instabilities developed in coexisting fluids associated with the plasma plume and its movement from the target to the support, also acquiring the effects of the instabilities already presented from the target in its immediate vicinity, in the first nanoseconds after each pulsed laser ignition of the ablation.

When ablation plasma starts cooling while getting closer to the substrate, liquid streams are generated in a complex condensation process, from mixed gas and liquid state clouds to crystalline growth (Figure 8 c2,c3). The droplets are grown on crystalline seeds that originate into the primary droplets developed under RTI on the target during ablation in a nucleation process, in the first nanoseconds. The primary droplets are trained into plasma motion, cooling in time up to the solid state, as monocrystals.

(d) In the deposition chamber, the plasma travels from target to substrate on a path of 2 mm or 6 mm with a very high speed, of $6.3 \cdot 10^3$ m/s. At such value of speed, the plasma pushes the buffer air gases in its front and produces a pressure wave, which remains behind plasma. Plasma plume is a fluid phase that will allow the pressure wave (shock wave) to propagate through its mass leading to a harmonic constrain in plasma (Figure 8 d1 – d3) leading to RMI [35], followed by condensation into liquid streams and/or droplets (Figure 8 d4). Also, the very high speed of the plasma will develop a very high temperature, based on the Mach's number diagram with stagnation temperature [10]. The temperature achieved in this way is favorable to plasma phase existence that will cool only when the plasma plume expands enough that arrives to a density value where the pressure wavelength can't be produced anymore.

The droplets generated under the conditions described in the present paragraphs a), b) and c) will re-deposit and some will be entrained in the spray-less nozzle effect in the ablation plasma plume, contributing to the following phenomena and processes. These phenomena and processes include elastic collisions and return on the target or deposition on the walls of the vacuum chamber. The breaking of the fluid thread is believed to explain the formation of larger (main drops) and smaller (satellites) droplets observed in the SEM images in Figures 7a. It means that, when the flow of molten metal breaks-in a main drop that will still be attached to the main stream for a period of time by a thinner mass of liquid, it will break-up later, but in drops of smaller sizes, called satellite drops.

The ring – shaped droplets from SEM image (Figure 7a) are the result of crown splash. The mechanism consists, on the one side in "kinetic crown splash" based on the high kinetic energy of

 doi:10.20944/preprints202403.1717.v1

the droplets at the impact with the substrate, and on the other side in the existence of liquid state on the support from the previous layered particles and droplets and, in the latter case, the crown splash is the effect of an instability of RTI kind, or "RTI crown splash". The "kinetic crown" splash generates rings disposed on the surface and the "RTI crown splash" generates craters in the first layer, which is still in melted state. Heated substrate could enhance the crown splash effect because the film is kept in melted phase on the support during deposition.

The Ag-thin film morphology and deeply embossed topography indicated by the SEM and 3D, 2D and 1D images obtained during AFM analysis indicates a suitable surface for catalytic processes to take place.

In the SEM images on the silver thin film, the uniform dispersion of the RB21 can be noticed (Figure 9a). In Figure 9a, the shape of the droplets can be distinguished, just like in the SEM image of the thin silver film in Figure 7a, but the image is darker and matte because of the organic material that covers the thin silver layer. No brightness differences are observed on the studied surface, compared to the SEM image of the thin silver layer in Figure 7a, where the droplets are brighter than the background. Higher magnitude of the image evidenced large crystalline structures (Figure 9b). The crystal structure in Figure 9b belongs to the components resulting from reaction between RB21 and NaHCO3 in the aqueous solution poured on the silver thin film.

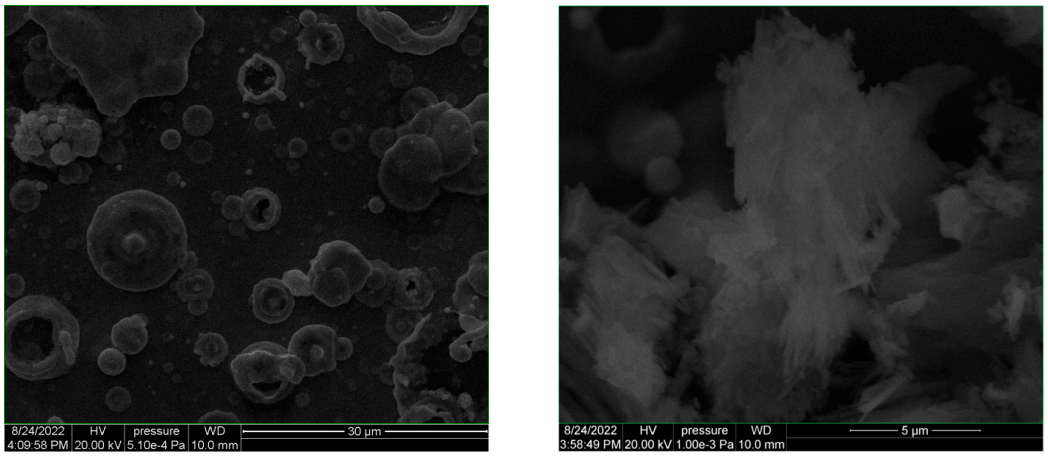

(a) (b)

Figure 9. SEM images of the silver thin film after interaction with the RB21 solution.

In the FTIR spectra of Figure 10, the high decomposition of the RB21 dyestuff (chemical structure shown in Figure 11) in RB21 solution is observed on the Q-Ag and R-Ag samples. The changes of the functional groups are identified in the FTIR spectra (Figure 10) using previous literature [36–39] compared to the initial structure of the RB21. The vibration bands assignments are presented in Table 2.

 doi:10.20944/preprints202403.1717.v1

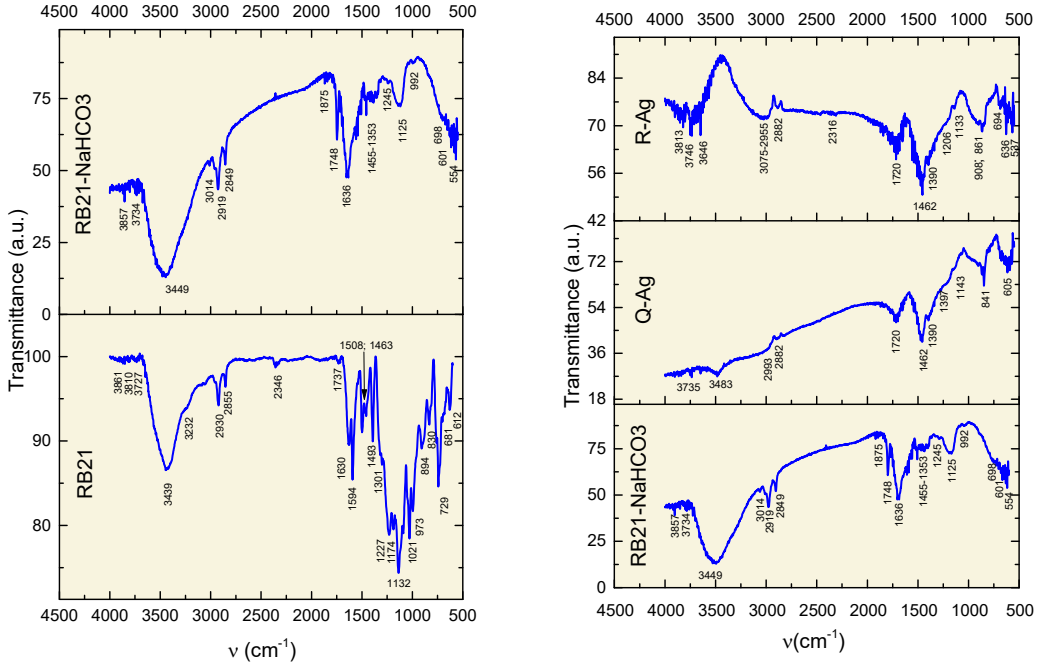

Figure 10. FTIR spectra of the initial dyestuff CI: RB21 (RB21); dried aqueous solution of RB21with $NaHCO_3$ (RB21-$NaHCO_3$); dried reacted RB21 solution under catalytic effect of the Ag-thin film (R-Ag) and dried RB21 solution leakage after interaction with the Ag-thin film.

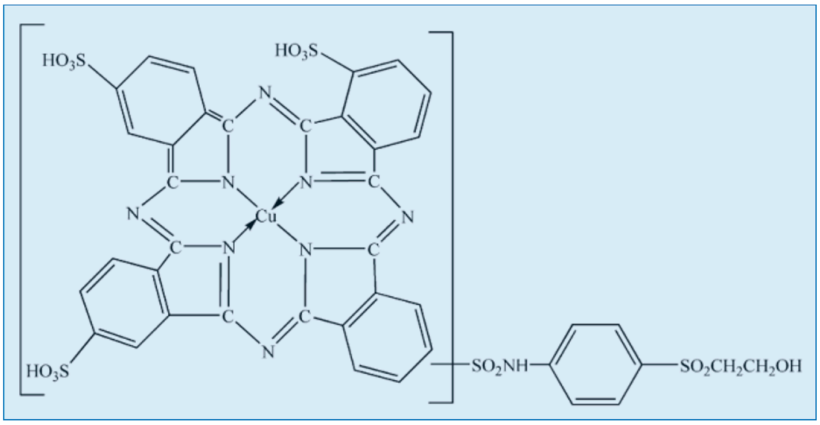

Figure 11. Chemical structure of Reactive Blue 21 dyestuff.

Table 2. Vibration bands of the functional groups.

RB21	**RB21-$NaCO_3$**	**R-Ag (dried *RB21-$NaCO_3$ aq after interaction with Ag-thin film)***	**Q-Ag (*dried leakage of RB21-$NaCO_3$)***	**Comments**
3861; 3810 v.w.	3857 v.w.	3813 v.w.		O-H free str.
3727 v.w.	3734 v.w.	3746 v.w.	3735 v.w.	O-H free str.
		3646 v.w.		O-H free str.
3439 s.	3449 s.	-	3483 v.w	O-H and N-H free and H-bonded str.
3232 sh.				N-H
	3014 v.w.	3075-2955 m.		C-H in aromatic/alkenes

 doi:10.20944/preprints202403.1717.v1

2930 m.	2919 m.		2993 m.	C-H alifatic
2855 m.	2849 m.	2882 m.	2883 m.	C-H alifatic
2346 w.		2316 w.		O=C=O carbon dioxide
	1875 w.			C=O stretching
1737 w.	1748 m.	1720 m.	1720 m.	C=O stretching in carbonate CO_3^{-2}
1630 s.	1636 s.			C-H aromatic; N-H bending; SO_3
1594 s.	-	-	-	Ring skeleton in pyrrole group; N-H bending in sulfonamide group
1508 s.	-	-	-	N-H bending in sulfonamide group
1493s.	-	-	-	C in heterocycles
1463 s.	1455 w.	1462 s.	1462 s.	C-C in heterocycles; C=O in $(COO)^-$; C-H aliphatic bending; CO_3^{-2} lattice vibrations
1301 s.	1353 w.	1390 m.	1390; 1397m.	S=O stretching asymmetric in SO_3 of sulfones in chromophore and sulfonamides in chromogen
1227 v.s.	1245v.w.	1206 sh.	-	C-N stretching in amines; C-O stretching in alcohols; S=O stretching symmetric in SO_3 in chromophore
1174 v.s.	1125 m.	1133 w.	1143 sh.	SO_2 in chromogen
1021 v.s.	-	-	-	C-N bending
973 v.s.	992v.w.	908 m., wide	-	C=C bending
894 s.	-	861 m.	-	C=C bending; S-O stretching
830 m.	-	-	841 m. sharp	N-H bending in sulfonamides; C=C bending; S-O stretching
729 s.	-	-	-	N-H bending; S-O stretching
681 m.	698 m.	694 w.	-	S-O stretching
612 m	601 m.	636 m. sharp	605 m. (multiple peaks	S-O stretching
-	554 m.	537 m. sharp	-	S-O stretching

Decomposition starts right after RB21 solution interaction with the silver thin film, proved by the changes in Q-Ag and R-Ag spectra. Carbonate (CO_3^{-2}) groups are evidenced by the 1748 cm^{-1} and 1462 cm^{-1} bands; the latter also indicates the lattice modes. The crystalline structure of the Q-Ag resulted compound, denoted by the ascending spectrum baseline, is also assigned to the carbonates as Mie scattering effect. Sulfonic (SO_3) groups are still intact (1390 cm^{-1}), while the aromatic rings are still present in R-Ag (3075 cm^{-1}), the same in the control test RB21-$NaHCO_3$ (3014 cm^{-1}). Aliphatic C-H is denoted in all samples by the bands at 2930 cm^{-1}, 2855 cm^{-1} (RB21); 2919 cm^{-1}, 2849 cm^{-1} (RB21-$NaHCO_3$); 2955 cm^{-1}, 2882 cm^{-1} (R-Ag and Q-Ag). The heteroaromatic rings with nitrogen and N-H in sulfonamides groups were largely affected, noted by severe transmission attenuation of the 3438 cm^{-1} (initial dye RB21) and 3449 cm^{-1} (RB21-$NaHCO_3$) vibration bands, becoming the very weak peak at 3483 cm^{-1} of Q-Ag dried leakage sample and missing in the R-Ag dried sample. Also, the skeleton vibrations at 1590 cm^{-1} assigned to pyrrole heteroatomic rings are missing in all treated samples and noticed only in the initial RB21 dye. The same band is assigned to N-H bending in sulfonamide group and its missing in RB21-$NHCO_3$, Q-Ag and R-Ag confirming modifications. Since the vibration bands at 3438 cm^{-1} (initial dye RB21), 3449 cm^{-1} (RB21-$NaHCO_3$), 3483 cm^{-1} (Q-Ag) and missing in the R-Ag also corresponds to the OH functional groups, it turns out that they were also modified compared to the initial molecule of the RB21 dye.

 doi:10.20944/preprints202403.1717.v1

Based on the chemical structure of the RB21 dye (Figure 11, the changes in the FTIR spectra of the studied samples (R-Ag and Q-Ag) in comparison with the reference samples (RB21 and RB21-$NaHCO_3$) indicate the following processes and reactions under silver thin film catalytic effect:

1. Sulfonyl group reaction with sodium bicarbonate, with increased rate under catalytic effect of Ag-thin film

$$D\text{-}SO_3H + Na^+H^+CO_3^{2-} \rightarrow D\text{-}SO_2\text{-}O^-Na^+ + CO_2 + H_2O. \quad (1)$$

The increased reaction rate is observed by the decrease in the intensity of the hydroxyl groups when comparing the FTIR spectra of the aqueous RB21-$NaHCO_3$ solution, dried on a glass plate with the R-Ag (aqueous RB21-$NaHCO_3$ solution dried on Ag thin film) and Q-Ag (leakage of aqueous RB21-$NaHCO_3$ over thin-filmed Ag and dried on glass). In the case of the R-Ag sample, the vibration of the hydroxyl groups is missing from the spectrum. This proves that they have been completely transformed.

2. Deprotonation of the sulfonamide group (SO_2-NH) due to the "nucleophilic attack" of CO_2 by amino group, reaction that requires a catalyst (usually Bronstad catalyst) [40].

$$D\text{-}SO_2\text{-}NH\text{-}Benz.\text{-}SO_2\text{-}CH_2\text{-}CH_2\text{-}OH + CO_2 \rightarrow R\text{-}SO_2\text{-}NCOOH\text{-}Benz.\text{-}SO_2\text{-}CH_2\text{-}CH_2\text{-}OH. \quad (2)$$

3. Dehydration at the level of the terminal hydroxyl group in the side chain led to the formation of the vinyl group. Usually, the reaction of sodium bicarbonate with alcoholic hydroxyl groups does not occur, because the first is a weak acid in this case (amphoteric character), while the second is a weak base. The lack of specific vibrations for the hydroxyl groups in the case of the R-Ag sample and their reduction in the case of the Q-Ag shows the damage of all OH groups in the dye molecule, resulting in the thin Ag film catalyzing the chemical process.

$$R\text{-}SO_2\text{-}NCOOH\text{-}Benz.\text{-}SO_2\text{-}CH_2\text{-}CH_2\text{-}OH \rightarrow R\text{-}SO_2\text{-}NCOOH\text{-}Benz.\text{-}SO_2\text{-}CH{=}CH_2 + H_2O. \quad (3)$$

4. Also, the FTIR spectra indicate changes in the aromatic and heteroaromatic structures when the RB21 and NaHCO3 dye solution comes in contact with the thin silver film.

The silver layer strong roughness due to ring shaped particles is evidenced with profilometry measurements and the profiles are presented in Figures 12a,b, while the reduced thickness after catalytic interaction is noticed in Figure 12c. The density of the peaks is lower after RB21 solution was added and there are cavities between peaks, proving that the RB21 solution had an effect of "etching" on the thin layer. The effect shows that some of the silver thin film material was consumed. This etching effect could be caused by entrainment of submicrometer silver particles in the resulting leakage as a result of pouring the aqueous solution of RB21 and $NaHCO_3$ and/or binding of silver particles to modified and ionized functional groups such as sulfonate and carboxylate.

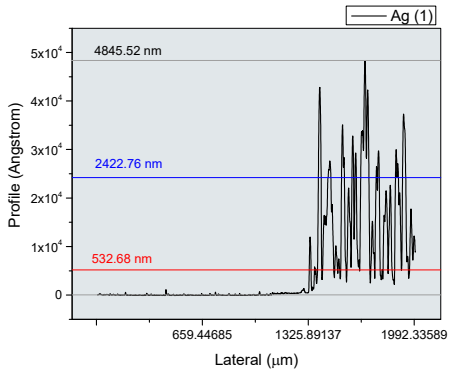

(a)

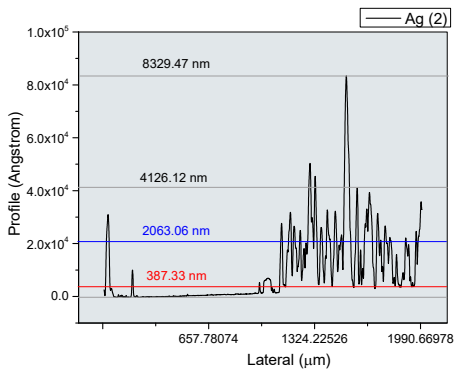

(b)

 doi:10.20944/preprints202403.1717.v1

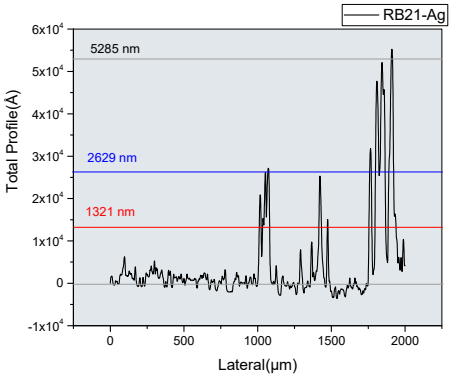

(c)

Figure 12. Silver thin film profile before (a,b) and after (c) interaction with RB21 solution.

On the optical microscope image in Figure 13a, a compact structure is observed, while in the image of Figure 13b darker areas are noticed, probably due to clogging with reaction products during the interaction with the RB21 solution. The size of the observed area is 1.4 x 1.1 mm, as can be measured on the grid of 0.1 x 0.1 mm attached with the image of the thin film.

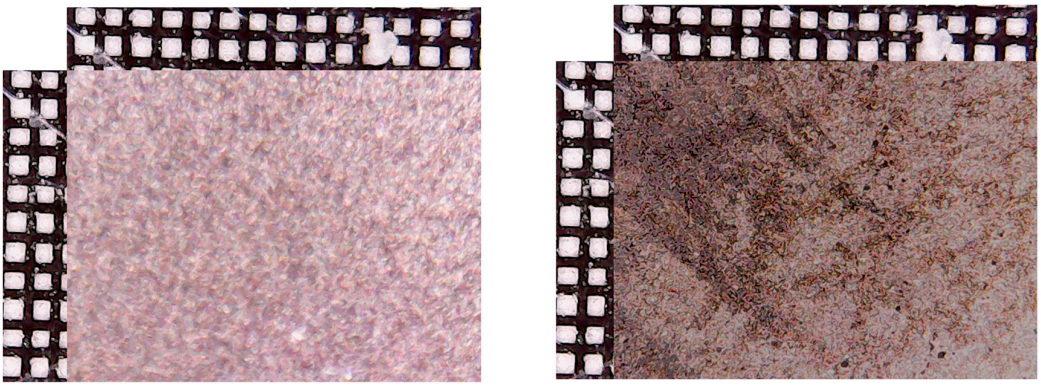

(a) (b)

Figure 13. Optical microscope image of the silver thin film before (a) and after (b) interaction with RB21 solution. The image is scaled by the grid of 0.1 x 0.1 mm.

4. Conclusions

The results of the study carried out in this work demonstrate the catalytic action of silver thin films of high roughness in catalytic decomposition processes of some organic compounds with complex molecules. The fluid instabilities (PRI = Plateau – Rayleigh instability; RTI = Rayleigh – Taylor instability; RMI = Richtmyer – Meshkov instability) induced by the use of high energy laser radiation led to obtaining the thin films of high roughness. Also, the study provides a fundamental approach to the phenomena and processes that led to obtaining the crystalline structure of the silver thin film produced by the PLD technique on a substrate at ambient temperature (without heating the substrate). The analysis by mass spectrometry using the pulsed laser with an energy of 30 mJ/pulse as the ionization source highlighted the role of boron in reaching the silver ionization energy threshold, also confirmed by the simulation results in COMSOL.

Author Contributions: All authors contributed equally to all activities related to this article. All authors have read and agreed to the published version of the manuscript.

Funding: This work was supported by a grant of the Ministry of Research, Innovation and Digitization, CNCS - UEFISCDI, project number PN-III-P1-1.1-PD-2021-0208, PD 53, within PNCDI III and Operational Program Competitiveness 2014–2020, Axis 1, under POC/448/1/1 research infrastructure projects for public R&D

institutions/Section F 2018, through the Research Center with Integrated Techniques for Atmospheric Aerosol Investigation in Romania (RECENT AIR) project, under grant agreement MySMIS No. 127324.

Data Availability Statement: The data presented in this study are available on request from the corresponding author on reasonable request.

Acknowledgments: We express our thanks to Stephen Haywood, test and installation engineer at Hiden Analytical, United Kingdom, for technical assistance during the measurements with the mass spectrometer.

Conflicts of Interest: The authors declare no conflicts of interest.

References

1. Anabitarte, F.; Cobo, A.; Lopez-Higuera, J.M. Laser-Induced Breakdown Spectroscopy: Fundamentals, Applications, and Challenges. *Int. Sch. Res. Notices* **2012**, *2012*, 285240. https://doi.org/10.5402/2012/285240
2. Tango, W.J.; Link, J.K.; Zare, R.N. Spectroscopy of K_2 Using Laser-Induced Fluorescence. *J. Chem. Phys.* **1968**, *49*, 4264-4268. https://doi.org/10.1063/1.1669869
3. Aguilera, J.A.; Aragón, C.; Peñalba, F. Plasma shielding effect in laser ablation of metallic samples and its influence on LIBS analysis. *Appl. Surf. Sci.* **1998**, *127–129*, 309–314. https://doi.org/10.1016/S0169-4332(97)00648-X
4. Fazio, B.; Trusso, S.; Fazio, E.; Neri, F.; Ossi, P.M.; Santo, N. Nanostructured silver thin films deposited by pulsed laser ablation. *Radiat. Eff. Defects Solids* **2008**, *163*, 673-683. https://doi.org/10.1080/10420150701781001
5. Machmudah, S.; Wahyudiono; Kuwahara, Y.; Sasaki, M.; Goto, M. Pulsed laser ablation in pressurized CO2 for nanoparticles fabrication. In Proceedings of the TENCON 2011 – 2011 IEEE Region 10 Conference, Bali, Indonesia, 21-24 November 2011, pp. 792-796. https://doi.org/10.1109/TENCON.2011.6129219
6. Mohammed, A.Z.; Menazea, A.A.; Mostafa, A.M.; Al-Ashkar, E.A. Ultra-thin silver nanoparticles film prepared via pulsed laser deposition: Synthesis, characterization, and its catalytic activity on reduction of 4-nitrophenol. *Surf. Interfaces* **2020**, *19*, 100438. https://doi.org/10.1016/j.surfin.2020.100438
7. Becker, J.S.; Jakubowski, N. The synergy of elemental and biomolecular mass spectrometry: new analytical strategies in life sciences. *Chem. Soc. Rev.* **2009**, *38*, 1969-1983. https://doi.org/10.1039/b618635c
8. Gurlui, S.; Sanduloviciu, M.; Strat, M.; Strat, G.; Mihesan, C.; Ziskind, M.; Focsa, C. Dynamic space charge structures in high fluence laser ablation plumes. *J. Optoelectron. Adv. Mater.* **2006**, *8*, 148-151.
9. Alonso, J.C.; Diamant, R.; Castillo, P.; Acosta–García, M.C.; Batina, N.; Haro-Poniatowski, E. Thin films of silver nanoparticles deposited in vacuum by pulsed laser ablation using a YAG:Nd laser. *Appl. Surf. Sci.* **2009**, *255*, 4933-4937. https://doi.org/10.1016/j.apsusc.2008.12.040
10. Stafe, M.; Vladoiu, I.; Negutu, C.; Popescu, I.M. Experimental investigation of the nanosecond laser ablation rate of aluminum. *Rom. Rep. Phys.* **2008**, *60*, 789-796.
11. Cocean, A.; Cocean, I.; Gurlui, S.; Iacomi, F. Study of the pulsed laser deposition phenomena by means of Comsol Multiphysics. *U.P.B. Sci. Bull. A* **2017**, *79*, 263-274.
12. Cocean, A.; Cocean, I.; Gurlui, S. Influence of the impurities to the composite materials in laser ablation phenomena, *U.P.B. Sci. Bull. A* **2021**, *83*, 225-238.
13. Cocean, A.; Cocean, I.; Cocean, G.; Postolachi, C.; Pricop, D.A.; Munteanu, B.S.; Cimpoesu, N.; Gurlui, S. Study of Physico-Chemical Interactions during the Production of Silver Citrate Nanocomposites with Hemp Fiber. *Nanomaterials* **2021**, *11*, 2560. https://doi.org/10.3390/nano11102560
14. Yang, Y.; Long, C.-L.; Yang, Z.-G.; Li, H.-P.; Wang, Q. Characterization and Determination of Silver Nanoparticle Using Single Particle-Inductively Coupled Plasma-Mass Spectrometry. *Chinese J. Anal. Chem.* **2014**, *42*, 1553-1560. https://doi.org/10.1016/S1872-2040(14)60777-5
15. Becker, J.S.; Becker, J.S. Imaging of metals, metalloids, and non-metals by laser ablation inductively coupled plasma mass spectrometry (LA-ICP-MS) in biological tissues. *Methods Mol Biol.* **2010**, *656*, 51-82. https://doi.org/10.1007/978-1-60761-746-4_3
16. Wu, B.; Zoriy, M.; Chen, Y.; Becker, J.S. Imaging of nutrient elements in the leaves of Elsholtzia splendens by laser ablation inductively coupled plasma mass spectrometry (LA-ICP-MS). *Talanta* **2009**, *78*, 132-137. https://doi.org/10.1016/j.talanta.2008.10.061
17. Pisonero, J.; Günther, D. Femtosecond laser ablation inductively coupled plasma mass spectrometry: fundamentals and capabilities for depth profiling analysis. *Mass Spectrom. Rev.* **2008**, *27*, 609-623. https://doi.org/10.1002/mas.20180
18. Seaman, C. Laser Ablation Inductively Coupled Plasma Mass Spectrometry Imaging of Plant Metabolites. *Methods Mol. Biol.* **2017**, *1618*, 125-135. https://doi.org/10.1007/978-1-4939-7051-3_11
19. Gurlui, S.; Agop, M.; Nica, P.; Ziskind, M.; Focsa, C. Experimental and theoretical investigations of a laser produced aluminum plasma, *Phys. Rev. E* **2008**, *78*, 026405. https://doi.org/10.1103/PhysRevE.78.026405

20. Cocean, I.; Cocean, A.; Postolachi, C.; Pohoata, V.; Cimpoesu, N.; Bulai, G.; Iacomi, F.; Gurlui, S. Alpha keratin amino acids BEHVIOR under high FLUENCE laser interaction. Medical applications. *Appl. Surf. Sci.* **2019**, *488*, 418-426. https://doi.org/10.1016/j.apsusc.2019.05.207
21. Cook, M.M.; Lander, J.A. Use of Sodium Borohydride to Control Heavy Metal Discharge in the Photographic Industry. *J. Appl. Photogr. Eng.* **1979**, *5*, 144-147.
22. Cotton, F.A.; Wilkinson, G. *Advanced Inorganic Chemistry*, 4th ed.; Interscience: New York, USA, 1980.
23. Lide, D.R. (Ed.) Handbook of Chemistry and Physics, 73rd ed.; CRC Press: Boca Raton, FL, USA, 1992; pp. 10-211.
24. NIST Chemistry WebBook. Available online: https://webbook.nist.gov/cgi/cbook.cgi?ID=C7440224&Units=SI&Mask=20#Ion-Energetics (accessed on 10 January 2024).
25. NIST Chemistry WebBook. Available online: https://webbook.nist.gov/cgi/cbook.cgi?ID=C7439896&Units=SI&Mask=20#Ion-Energetics (accessed on 10 January 2024).
26. NIST Chemistry WebBook. Available online: https://webbook.nist.gov/cgi/cbook.cgi?ID=C7440020&Units=SI&Mask=20#ref-5 (accessed on 10 January 2024).
27. NIST Chemistry WebBook. Available online: https://webbook.nist.gov/cgi/cbook.cgi?ID=C7440428&Units=SI&Mask=20#Ion-Energetics (accessed on 10 January 2024).
28. Cocean, A.; Pelin, V.; Cazacu, M.M.; Cocean, I.; Sandu, I.; Gurlui, S.; Iacomi, F. Thermal Effects Induced by Laser Ablation in Non-Homogeneous Limestone Covered by an Impurity Layer. *Appl. Surf. Sci.* **2017**, *424*, 324-329. https://doi.org/10.1016/j.apsusc.2017.03.172
29. Jyoti, K.; Baunthiyal, M.; Singh, A. Characterization of silver nanoparticles synthesized using *Urtica dioica* Linn. leaves and their synergistic effects with antibiotics. *J. Radiat. Res. Appl. Sci.* **2015**, *9*, 217-227. https://doi.org/10.1016/j.jrras.2015.10.002
30. Bagherzade, G.; Tavakoli, M.M.; Namaei, M.H. Green synthesis of silver nanoparticles using aqueous extract of saffron (*Crocus sativus* L.) wastages and its antibacterial activity against six bacteria. *Asian Pac. J. Trop. Biomed.* **2017**, *7*, 227–233. https://doi.org/10.1016/j.apjtb.2016.12.014
31. Karthik, L.; Kumar, G.; Vishnu Kirthi, A.; Rahuman, A.A.; Bhaskara Rao, K.V. *Streptomyces* sp. LK3 mediated synthesis of silver nanoparticles and its biomedical application. *Bioprocess Biosyst. Eng.* **2014**, *37*, 261-267. https://doi.org/10.1007/s00449-013-0994-3
32. Hajakbari, F.; Ensandoust, M. Study of Thermal Annealing Effect on the Properties of Silver Thin Films Prepared by DC Magnetron Sputtering, *Acta Phys. Pol. A* **2016**, *129*, 680-682. https://doi.org/10.12693/APhysPolA.129.680
33. Taylor, G.I. The instability of liquid surfaces when accelerated in a direction perpendicular to their planes. I. *Proc. R. Soc. Lond. A* **1950**, *201*, 192-196. https://doi.org/10.1098/rspa.1950.0052
34. Chavaraddi, K.B.; Chandaragi, P.I.; Gouder, P.M.; Marali, G.B. Effect of Electromagnetic field on Rayleigh-Taylor instability in a power-law fluid in presence of boundary roughness. *J. Phys.: Conf. Ser.* **2021**, *1849*, 012019. https://doi.org/10.1088/1742-6596/1849/1/012019
35. Abarzhi, S.I.; Herrmann, M. New type of the interface evolution in the Richtmyer-Meshkov instability. Available online: https://ntrs.nasa.gov/api/citations/20040027954/downloads/20040027954.pdf (accessed on 19 March 2024).
36. Pretch, E.; Bülmann, P.; Badertscher, M. *Structure Determination of Organic Compounds. Tables of Spectral Data*, 4th ed.; Springer: Berlin, Germany, 2009.
37. Miller, F.A.; Wilkins, C.H. Infrared Spectra and Characteristic Frequencies of Inorganic Ions. Their Use in Qualitative Analysis. *Anal. Chem.* **1952**, *24*, 1253–1294. https://doi.org/10.1021/ac60068a007
38. Cocean, G.; Cocean, A.; Postolachi, C.; Garofalide, S.; Bulai, G.; Munteanu, B.S.; Cimpoesu, N.; Cocean, I.; Gurlui, S. High-Power Laser Deposition of Chitosan Polymers: Medical and Environmental Applications. *Polymers* **2022**, *14*, 1537. https://doi.org/10.3390/polym14081537
39. Cocean, G.; Cocean, A.; Garofalide, S.; Pelin, V.; Munteanu, B.S.; Pricop, D.A.; Motrescu, I.; Dimitriu, D.G.; Cocean, I.; Gurlui, S. Dual-Pulsed Laser Ablation of Oyster Shell Producing Novel Thin Layers Deposed to Saccharomyces cerevisiae. *Polymers* **2023**, *15*, 3953. https://doi.org/10.3390/polym15193953
40. Said, R.B.; Kolle, J.M.; Essalah, K.; Tangour, B.; Sayari, A. A Unified Approach to CO2–Amine Reaction Mechanisms. *ACS Omega* **2020**, *5*, 26125-26133. https://doi.org/10.1021/acsomega.0c03727